

Variable Basis Mapping for Real-Time Volumetric Visualization

Qibiao Li* Yuxuan Wang* Youcheng Cai[†] Huangsheng Du Ligang Liu

University of Science and Technology of China

caiyoucheng@ustc.edu.cn

Abstract

*Real-time visualization of large-scale volumetric data remains challenging, as direct volume rendering and voxel-based methods suffer from prohibitively high computational cost. We propose **Variable Basis Mapping (VBM)**, a framework that transforms volumetric fields into 3D Gaussian Splatting (3DGS) representations through wavelet-domain analysis. First, we precompute a compact Wavelet-to-Gaussian Transition Bank that provides optimal Gaussian surrogates for canonical wavelet atoms across multiple scales. Second, we perform analytical Gaussian construction that maps discrete wavelet coefficients directly to 3DGS parameters using a closed-form, mathematically principled rule. Finally, a lightweight image-space fine-tuning stage further refines the representation to improve rendering fidelity. Experiments on diverse datasets demonstrate that VBM significantly accelerates convergence and enhances rendering quality, enabling real-time volumetric visualization. The code will be publicly released upon acceptance.*

1. Introduction

Volumetric data are widely used across science and engineering, ranging from medical imaging (CT, MRI) [28, 39] to simulations in fluid dynamics [24, 34], climate [4], and planetary-scale systems [32]. Volume visualization is crucial for revealing patterns in such data and for providing users with an intuitive means of complex structures.

As the resolution and scale of volumetric data increase, traditional visualization methods, such as direct volume rendering [36], become computationally expensive and slow, hindering real-time interaction and flexible data exploration. Recently, 3D Gaussian Splatting (3DGS) [26] has emerged as a powerful technique for representing and rendering complex scenes. Unlike volumetric ray marching [37, 54] or voxel-based methods [7, 15, 16, 38, 47, 55],

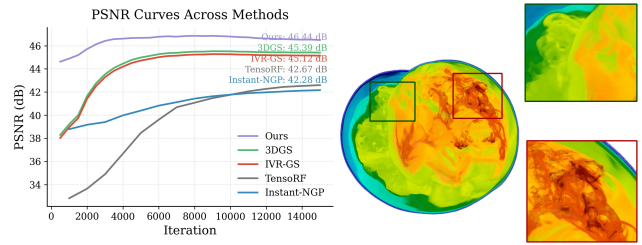


Figure 1. Left: Our excellent PSNR curve demonstrating the performance of the **VBM** framework on Supernova data. Right: The VBM-based Gaussian model effectively captures fine details.

3DGS achieves real-time photorealistic rendering using explicit, anisotropic 3D Gaussian primitives and analytical rasterization. From a functional perspective, this representation can be viewed as a projection of the radiance field—a mapping from \mathbb{R}^3 to \mathbb{R}^4 —onto a function space spanned by Gaussian basis functions. The optimal Gaussian approximation is obtained through an image-driven optimization, in which both initialization and the optimization trajectory determine the final quality and convergence speed.

In novel view synthesis, 3DGS typically relies on structure-from-motion (SfM) [43] for initialization. For volumetric visualization, iVR-GS [50] adopts randomly initialized Gaussian primitives, whereas VEG [13] employs a heuristic strategy in which each initial Gaussian is defined as a sphere whose size is proportional to the local point density. Sewell et al. [44] seek to enhance initialization by sampling points from isosurfaces to position the Gaussians more accurately, although isosurface extraction can be computationally expensive. Nevertheless, these approaches still suffer from two major limitations: (1) they are heuristic in nature and fail to exploit the rich structural and statistical information inherent in volumetric data; and (2) the construction of Gaussians relies heavily on computationally intensive image-space optimization, leading to high computational cost and slow convergence.

To overcome these limitations, we draw inspiration from the spatial–frequency decomposition of wavelets and leverage their multiresolution analysis of volumetric data to

*Equal contribution

[†]Corresponding author

obtain high-quality initializations for 3DGS, thereby enabling stable and efficient optimization. However, employing wavelet analysis introduces two significant challenges: (1) there exists a substantial representational gap between wavelet and Gaussian bases, which makes direct conversion nontrivial; and (2) a naïve implementation would incur cubic computational complexity in Wavelet-to-Gaussian transitions, resulting in prohibitive computational cost.

To address these issues, we propose a **Variable-Basis Mapping** (VBM) framework for efficient volumetric rendering in the wavelet domain. First, we precompute a compact **Wavelet-to-Gaussian Transition Bank**. For each wavelet kernel $\psi_{j,k}(x)$ at frequency level j and spatial position k , we obtain its optimal Gaussian approximation through a statistical estimation process. Although direct computation would require $J \times G^3$ individual transitions for a J -level wavelet transform, the translation covariance of wavelet bases allows us to compute only the canonical kernel $\psi_{j,k=(0,0,0)}$ for each level, where G denotes the volumetric data resolution. The remaining kernels can be derived analytically through translation and scaling, as guaranteed by the group representation theorem [1, 2]. Second, we propose an **analytical Gaussian construction** strategy that decomposes the volumetric field using the discrete wavelet transform (DWT) [20, 35], representing the volume as a linear combination of wavelet basis functions and their corresponding coefficients. By applying the precomputed Wavelet-to-Gaussian transitions, each wavelet basis is mapped analytically to a Gaussian basis, and the associated wavelet coefficients are systematically translated into the corresponding 3DGS parameters according to a principled mapping rule. Finally, an **image-space Gaussian fine-tuning** strategy refines the Gaussian parameters, ensuring visual consistency and convergence. Experimental results demonstrate that our method not only improves training efficiency but also achieves higher rendering quality than state-of-the-art approaches.

Our main contributions can be summarized as follows:

- To the best of our knowledge, **Variable Basis Mapping** is the first framework that establishes a direct, mathematical bridge between volumetric analysis and 3D Gaussian Splatting, laying a new foundation for efficient field-to-primitive conversion.
- We develop a principled kernel transition mechanism, named **Wavelet-to-Gaussian Transition Bank**, theoretically grounded in translation consistency, which enables efficient and reusable derivation of Gaussian bases.
- We introduce a **Paradigm Shift for Real-Time Volume Visualization**, that transforms traditional volumetric visualization into 3D Gaussian Splatting format. This “baking” process preserves volumetric semantics while inheriting 3DGS’s real-time rendering efficiency.

2. Related Work

Volumetric Representations and Rendering. Volumetric data are central to scientific visualization, computer graphics, and medical imaging. Traditional Direct Volume Rendering [36] integrates radiance along viewing rays for physically accurate visualization but is computationally expensive due to dense sampling requirements.

To improve scalability, hierarchical data structures such as Sparse Voxel Octrees [19, 31, 40], multi-resolution pyramids [49, 51], and bricked grids [14, 22] enable adaptive resolution and memory-efficient rendering.

Rendering efficiency has also benefited from more effective sampling strategies. Importance sampling [29, 30, 33, 52] focuses computation on radiometrically or perceptually salient regions, while learned selective rendering [5, 48] reconstructs full images from sparsely rendered content.

Neural Scene Representations. Recent advances in neural radiance field, such as NeRF [37], Plenoxel [15], TensoRF [7], InstantNGP [38], and K-Planes [16], have enabled compact and high-fidelity representations for novel view synthesis. Building upon these implicit approaches, 3D Gaussian Splatting (3DGS) [26] represents a scene using anisotropic Gaussian primitives that are both differentiable and efficient to render, bridging volumetric and explicit representations. Extensions that incorporate Gaussians into mesh-based framework, such as SuGaR [21], GaussianMesh [17], GaMeS [53], and MeshGS [10], enhance surface fidelity by aligning or attaching Gaussian distributions to mesh surfaces or vertices, leveraging local geometry for improved accuracy.

For volumetric modeling, IVR-GS [50] initializes Gaussians randomly and optimizes them entirely in image space, while VEG [13] heuristically distributes Gaussian scales according to local density. Sewell et al. [44] further employ isosurface-based point clouds for high-quality ambient occlusion. However, these methods remain largely heuristic and fail to leverage the inherent structural and statistical regularities of volumetric data. In contrast, our approach establishes a principled mapping from volumetric field to Gaussian primitives, within a wavelet-informed framework.

Wavelet Analysis in Volumetric Data Processing.

Wavelet analysis [12, 35] offers a multiresolution representation with joint spatial–frequency localization, outperforming global transforms such as the Fourier [46]. Wavelets have been widely applied to volumetric compression [6, 23, 27], denoising [8, 9, 25], and feature extraction [18, 41].

Beyond volumetric settings, wavelets have demonstrated broad utility in image processing [3, 20], time-series analysis [11, 42], and modern deep learning pipelines [56, 57], underscoring their versatility for hierarchical, frequency-aware signal modeling.

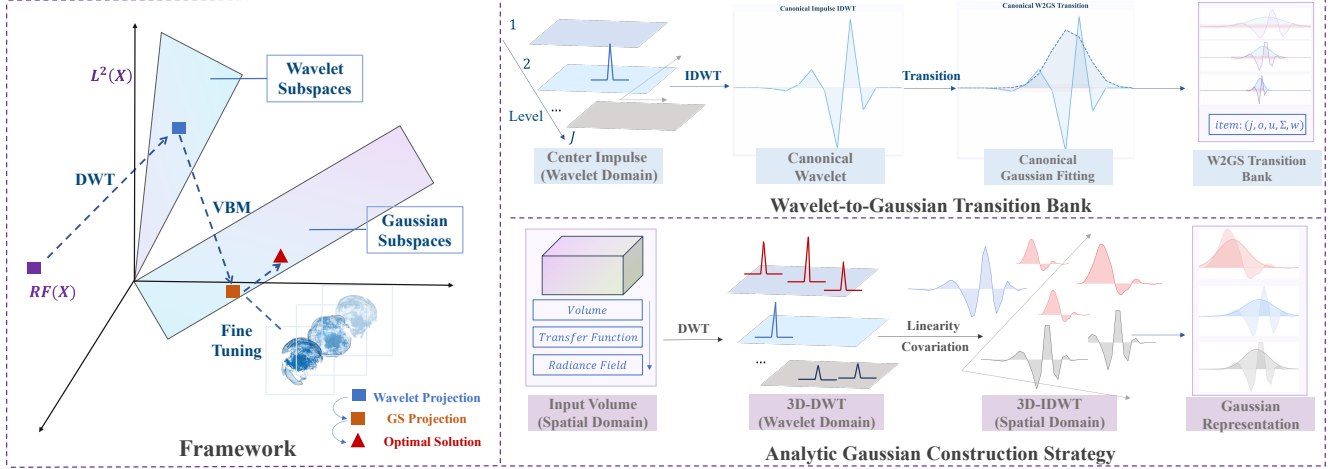


Figure 2. Overview of the *VBM* framework. A volumetric radiance field is projected onto the wavelet subspace using discrete wavelet transform (DWT), and then mapped to the function subspace spanned by Gaussian primitives. This is followed by efficient image-space fine-tuning to obtain the optimal parameters. The process is supported by the Wavelet-to-Gaussian Transition Bank, built from canonical wavelets and Gaussians, and an analytic Gaussian construction strategy leveraging the linearity and translation consistency of the IDWT.

3. Preliminaries

Transfer Function. Scientific visualization maps spatial or spatio-temporal data into perceptually meaningful visual representations. Given a spatial domain $D \subset \mathbb{R}^d$, the dataset is modeled as a field $F : D \rightarrow \mathbb{R}^r$, where r denotes the value dimension. A *transfer function* $TF : \mathbb{R}^r \rightarrow \mathbb{R}^n$ transforms physical quantities into visual attributes of a radiance field, typically producing an RGBA vector (c, α) . In this paper, we discretize D into a uniform grid of resolution G^3 , yielding $F \in \mathbb{R}^{G \times G \times G \times r}$. Applying the transfer function produces the radiance volume: $RF = TF(F) \in \mathbb{R}^{G \times G \times G \times 4}$, yielding the volume rendered downstream.

3D Wavelet Transform. The wavelet transform provides joint spatial–frequency localization, enabling compact and structured representations of volumetric fields. Given a mother wavelet $\psi(\cdot)$ and a scaling function $\phi(\cdot)$, the dyadic atoms are defined as:

$$\psi_{j,\mathbf{k}}(\mathbf{x}) = 2^{3j/2} \psi(2^j \mathbf{x} - \mathbf{k}). \quad (1)$$

where \mathbf{x} denotes the spatial position, j is the scale index, and $\mathbf{k} = (k_x, k_y, k_z)$ is the spatial translation index.

Each channel i of a vector-valued radiance field $RF^{(i)}(\mathbf{x})$ can be expressed as a multiresolution expansion:

$$RF^{(i)}(\mathbf{x}) = \sum_{\mathbf{k}} c_{0,\mathbf{k}}^{(i)} \phi(\mathbf{x} - \mathbf{k}) + \sum_{j=0}^{J-1} \sum_{\mathbf{k}} d_{j,\mathbf{k}}^{(i)} \psi_{j,\mathbf{k}}(\mathbf{x}), \quad (2)$$

where $c_{0,\mathbf{k}}^{(i)} = \langle RF^{(i)}, \phi(\mathbf{x} - \mathbf{k}) \rangle$, $d_{j,\mathbf{k}}^{(i)} = \langle RF^{(i)}, \psi_{j,\mathbf{k}} \rangle$ are the low- and high-frequency coefficients, respectively. Here, J denotes the number of decomposition levels in the wavelet transform. Accordingly, the radiance field $RF(\cdot)$

can be expressed in a compact multi-scale form using the 3D wavelet transform:

$$RF(\mathbf{x}) \approx \sum_{j=0}^J \sum_{\mathbf{k} \in D} \begin{bmatrix} \mathbf{c}_{j,\mathbf{k}} \\ \alpha_{j,\mathbf{k}} \end{bmatrix} \psi_{j,\mathbf{k}}(\mathbf{x}), \quad (3)$$

where the coefficient vectors $\mathbf{c}_{j,\mathbf{k}} = \langle \mathbf{c}, \psi_{j,\mathbf{k}} \rangle$ and $\alpha_{j,\mathbf{k}} = \langle \alpha, \psi_{j,\mathbf{k}} \rangle$ encode the color and opacity at different scales.

3D Gaussian Splatting. 3DGS [26] represents the radiance field as a collection of N anisotropic Gaussian kernels:

$$\mathcal{G} = \{(\boldsymbol{\mu}_i, \boldsymbol{\Sigma}_i, \mathbf{c}_i, \alpha_i)\}_{i=1}^N, \quad (4)$$

where $\boldsymbol{\mu}_i \in \mathbb{R}^3$ denotes the center, $\boldsymbol{\Sigma}_i \in \mathbb{R}^{3 \times 3}$ represents the covariance matrix, \mathbf{c}_i is the color, and α_i is the opacity.

The radiance field can be approximated by a weighted linear combination of anisotropic Gaussian primitives:

$$RF(\mathbf{x}) \approx \sum_{i=1}^N \begin{bmatrix} \mathbf{c}_i \\ \alpha_i \end{bmatrix} \exp\left[-\frac{1}{2}(\mathbf{x} - \boldsymbol{\mu}_i)^\top \boldsymbol{\Sigma}_i^{-1}(\mathbf{x} - \boldsymbol{\mu}_i)\right]. \quad (5)$$

This linear combination over localized Gaussian primitives enables an efficient and differentiable approximation of the radiance distribution, while supporting real-time rendering.

4. Method

4.1. Formulation and Overview

We cast *Variable Basis Mapping* as a sequence of functional mapping connecting the physical field, its visual encoding, and final primitive representation. Given a physical field F ,

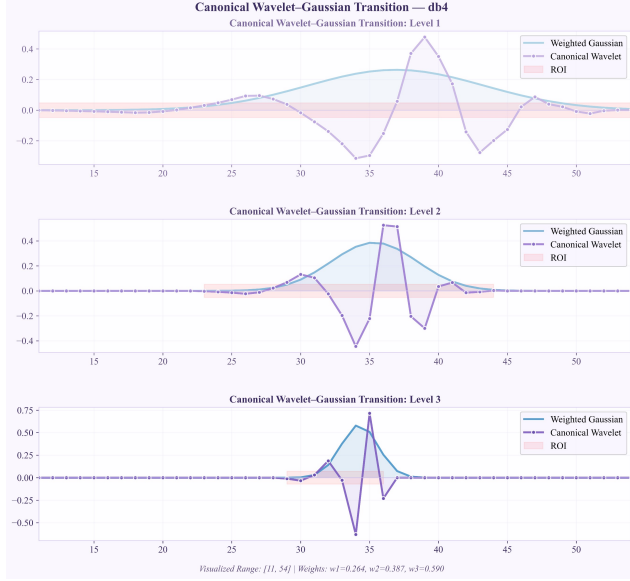


Figure 3. Wavelet-to-Gaussian Transition Bank. Illustration of the transition from localized wavelet kernels to Gaussian primitives across multiple scales.

we first apply a transfer function TF to obtain a radiance field RF . The radiance field is then decomposed into its multi-scale wavelet representation Φ , which is subsequently converted into a set of 3D Gaussian primitives \mathcal{G} . The overall mapping is summarized as: $F \xrightarrow{TF} RF \rightarrow \Phi \rightarrow \mathcal{G}$.

We have established an efficient correspondence between wavelets and their optimal Gaussian counterparts:

$$\psi_{j,\mathbf{k}}(\mathbf{x}) \sim g_{j,\mathbf{k}}(\mathbf{x}). \quad (6)$$

Substituting Eq. (6) into Eq. (3), we obtain:

$$RF(\mathbf{x}) \approx \sum_{j=0}^{J-1} \sum_{\mathbf{k}} [\mathbf{c}_{j,\mathbf{k}}, \alpha_{j,\mathbf{k}}]^\top g_{j,\mathbf{k}}(\mathbf{x}), \quad (7)$$

where $[\mathbf{c}_{j,\mathbf{k}}, \alpha_{j,\mathbf{k}}]^\top = (R, G, B, \alpha)^T$ denotes the color and opacity coefficients, jointly determined by the wavelet subband intensity and an analytically derived parameter mapping rule. This formulation directly yields the Gaussian representation \mathcal{G} of the volumetric field.

Overview. Our goal is to exploit the information of volume to construct Gaussian primitives directly, thereby enabling efficient real-time rendering and optimization. We first develop a Wavelet-to-Gaussian Transition Bank, which provides precomputed Gaussian approximations for canonical wavelet kernels (Sec. 4.2). Next, we apply a 3D discrete wavelet transform (DWT) to the radiance field to extract its spatial-frequency characteristics, and leveraging the transition bank, derive a Gaussian-splatting expansion via a simple lookup operation (Sec. 4.3). Finally, a lightweight

image-space fine-tuning stage refines the resulting 3DGS representation, enabling real-time volumetric visualization (Sec. 4.4). See Fig. 2 for an overview of the process.

4.2. Wavelet-to-Gaussian Transition Bank

We develop an efficient procedure to construct Gaussian surrogates for wavelet kernels, as depicted in Fig. 3. Given a J -level wavelet transform applied to the radiance field RF , a straightforward approach would independently fit an optimal Gaussian to every wavelet kernel across all scales and spatial positions, leading to $J \times G^3$ fittings. However, within each subband, all wavelet kernels are identical up to translation. Thus, it is sufficient to fit a *single* canonical Gaussian per subband, and obtain others via spatial translation.

Concretely, our procedure consists of four steps: (i) define a *canonical wavelet kernel*, (ii) derive its *translation rule* to arbitrary spatial locations, (iii) fit an optimal Gaussian to the canonical kernel, and (iv) translate the fitted parameters to generate approximations for any kernel within the same subband. This yields a compact yet expressive Wavelet-to-Gaussian Transition Bank that supports analytical conversion from wavelet bases to Gaussian primitives.

Canonical Wavelet Construction. We define the canonical wavelet kernel as the spatial footprint of a unit impulse in the wavelet domain. Let \mathcal{W} denote the 3D discrete wavelet transform (DWT) with J decomposition levels. At each level j , subbands are indexed by:

$$\mathbf{o} = (o_x, o_y, o_z) \in \{\mathbb{L}, \mathbb{H}\}^3, \quad (8)$$

where $o_d \in \{\mathbb{L}, \mathbb{H}\}$ indicates low- or high-pass filtering along axis $d \in \{x, y, z\}$. For instance, $\mathbf{o} = (\mathbb{L}, \mathbb{L}, \mathbb{H})$ corresponds to low-pass filtering on x, y , and high-pass on z .

Given a decomposition level j and orientation \mathbf{o} , we define an *impulse* in the corresponding subband as:

$$e_{j,\mathbf{o},\mathbf{k}=(k_x, k_y, k_z)}(\boldsymbol{\kappa}) = \begin{cases} 1, & \text{if } \boldsymbol{\kappa} = \mathbf{k} \text{ in subband } (j, \mathbf{o}), \\ 0, & \text{otherwise,} \end{cases} \quad (9)$$

where $\mathbf{k} = (k_x, k_y, k_z)$ denotes the spatial index.

Applying the inverse wavelet transform, \mathcal{W}^{-1} , to this one-hot feature yields its spatial-domain response. Further, by centering the impulse at $\mathbf{k} = (0, 0, 0)$, we obtain the *canonical wavelet*: $\hat{\psi}_{j,\mathbf{o}}(\mathbf{x})$:

$$\{\hat{\psi}_{j,\mathbf{o}}(\mathbf{x}) = \mathcal{W}^{-1}[e_{j,\mathbf{o},(0,0,0)}(\boldsymbol{\kappa})] \mid j, \mathbf{o}\}, \quad (10)$$

where $j \in \{0, \dots, J\}$, and $\mathbf{o} \in \{\mathbb{L}, \mathbb{H}\}^3$. The complete set $\{\hat{\psi}_{j,\mathbf{o}}(\mathbf{x})\}$ therefore contains $8(J+1)$ canonical wavelet kernels, each capturing a distinct scale–orientation pattern in the volumetric field.

Translation Consistency. We now establish translation consistency within each subband: all wavelet kernels in a

given subband are spatially translated replicas of the corresponding canonical kernel. Consider an arbitrary impulse in subband (j, \mathbf{o}) located at \mathbf{k} . Its spatial-domain response is given by:

$$\hat{\psi}_{j,\mathbf{o},\mathbf{k}}(\mathbf{x}) := \mathcal{W}^{-1}[e_{j,\mathbf{o},\mathbf{k}}](\mathbf{x}), \quad (11)$$

which can be derived from the canonical response at the same scale and orientation.

To formalize this relationship, we introduce the translation operator $(T_{\Delta}f)(\mathbf{x}) = f(\mathbf{x} - \Delta)$. Under approximately linear-phase filter banks, such as *biorthogonal* wavelets [12] with symmetric or periodic boundary extensions, the inverse DWT exhibits near-translation covariance on the discrete sampling grid:

$$\hat{\psi}_{j,\mathbf{o},\mathbf{k}}(\mathbf{x}) \approx (T_{2^j \mathbf{k} + \delta_{j,\mathbf{o}}} \hat{\psi}_{j,\mathbf{o}})(\mathbf{x}), \quad (12)$$

where $\delta_{j,\mathbf{o}}$ is a subpixel offset determined by the phase delay and half-sample shift of the analysis–synthesis filter pair. In practice, we use the biorthogonal 4.4 wavelet and set $\delta_{j,\mathbf{o}} \approx (\frac{1}{2}, \frac{1}{2}, \frac{1}{2})$.

This property guarantees that all wavelets sharing the same scale j and orientation \mathbf{o} are spatially consistent translations of the canonical response $\hat{\psi}_{j,\mathbf{o}}(\mathbf{x})$. Consequently, Gaussian primitives fitted to the canonical kernel can be efficiently propagated across spatial positions through simple translation, eliminating the need for redundant parameter fitting for each wavelet instance.

Transition Bank Construction. Here, we approximate the canonical wavelet kernel with a single Gaussian primitive. The aim is to match the canonical wavelet’s dominant spatial footprint with a Gaussian envelope, a procedure we term *dominant-lobe estimation*. Given the canonical wavelet kernel $\hat{\psi}_{j,\mathbf{o}}(\mathbf{x})$ we first compute a normalized magnitude distribution:

$$W(\mathbf{x}) = \frac{|\hat{\psi}_{j,\mathbf{o}}(\mathbf{x})|}{\sum_{\mathbf{u} \in D} |\hat{\psi}_{j,\mathbf{o}}(\mathbf{u})|},$$

$$\mathcal{R} = \{\mathbf{x} \in D : W(\mathbf{x}) > \tau \max_{\mathbf{u} \in D} W(\mathbf{u})\}, \quad (13)$$

where $\tau \in (0, 1)$ is the relative threshold that defines *the region of interest* (ROI) corresponding to the dominant lobe. Within this ROI, we estimate the centroid and covariance of the kernel from the first- and second-order weighted moments:

$$\mathbf{u}_{j,\mathbf{o}} = \frac{\sum_{\mathbf{x} \in \mathcal{R}} W(\mathbf{x}) \mathbf{x}}{\sum_{\mathbf{x} \in \mathcal{R}} W(\mathbf{x})},$$

$$\Sigma_{j,\mathbf{o}} = \frac{\sum_{\mathbf{x} \in \mathcal{R}} W(\mathbf{x}) (\mathbf{x} - \mathbf{u}_{j,\mathbf{o}})(\mathbf{x} - \mathbf{u}_{j,\mathbf{o}})^{\top}}{\sum_{\mathbf{x} \in \mathcal{R}} W(\mathbf{x})}. \quad (14)$$

These two parameters define the geometry of the canonical Gaussian approximation:

$$\{g_{j,\mathbf{o}}(\mathbf{x}) = \exp\left(-\frac{1}{2}(\mathbf{x} - \mathbf{u}_{j,\mathbf{o}})^{\top} \Sigma_{j,\mathbf{o}}^{-1}(\mathbf{x} - \mathbf{u}_{j,\mathbf{o}})\right) \mid j, \mathbf{o}\}. \quad (15)$$

Energy Conservation. To preserve energy between each wavelet kernel and its Gaussian approximation, we introduce a weight vector $\mathbf{w}_{j,\mathbf{o}} \in \mathbb{R}^4$ that rescales the Gaussian envelope to match the original wavelet energy. The scalar weight $w_{j,\mathbf{o}}$ is obtained minimizing the L^2 discrepancy between the wavelet magnitude and the scaled Gaussian:

$$w_{j,\mathbf{o}} = \arg \min_w \|\|\hat{\psi}_{j,\mathbf{o}}\| - w g_{j,\mathbf{o}}\|_{L^2}, \quad (16)$$

where $\|\cdot\|_{L^2}$ denotes the Lebesgue L^2 norm [45]. In practice, let $\mathbf{Y}, \mathbf{G} \in \mathbb{R}^N$ be sampled magnitudes of $\hat{\psi}_{j,\mathbf{o}}$ and $g_{j,\mathbf{o}}$ within the ROI. We compute $w_{j,\mathbf{o}}$ by ridge regression:

$$w_{j,\mathbf{o}} = \arg \min_w \|\|\mathbf{Y}\| - w \mathbf{G}\|_2^2 + \lambda w^2, \quad (17)$$

where λ is a small regularization term. The resulting scalar is broadcast to four channels as $\mathbf{w}_{j,\mathbf{o}}$. The pair $(g_{j,\mathbf{o}}, \mathbf{w}_{j,\mathbf{o}})$ forms the canonical Gaussian. The complete transition bank is built as:

$$\{(\mathbf{w}_{j,\mathbf{o}}, g_{j,\mathbf{o}}(\mathbf{x})) \mid j, \mathbf{o}\}, \quad (18)$$

which maps each canonical wavelet kernel to its Gaussian counterpart: $\hat{\psi}_{j,\mathbf{o}} \rightarrow g_{j,\mathbf{o}}$. For $\hat{\psi}_{j,\mathbf{o},\mathbf{k}}$, the Gaussian approximation is retrieved by key (j, \mathbf{o}) and translated via

$$g_{j,\mathbf{o},\mathbf{k}}(\mathbf{x}) = (T_{2^j \mathbf{k} + \delta_{j,\mathbf{o}}} g_{j,\mathbf{o}})(\mathbf{x}), \quad (19)$$

which directly parallels the translation property in Eq.(12).

4.3. Analytical Gaussian Construction

We present an analytical formulation for directly representing a volumetric radiance field using Gaussian primitives. The process consists of four stages: (i) The discrete wavelet transform (DWT) is first applied to decompose the radiance field into multiscale subbands. (ii) Each wavelet coefficient is then associated with a Gaussian primitive that models its spatial footprint. (iii) Leveraging the linearity of the inverse DWT (IDWT), the spatial contributions of all coefficients within each subband are analytically aggregated. (iv) All subband-level Gaussian fields are combined to yield a complete Gaussian representation of the original radiance field.

Multichannel Wavelet Transform. The input volumetric radiance field is a four-channel function:

$$V : \mathbb{R}^3 \rightarrow \mathbb{R}^4, \quad V(\mathbf{x}) = [R(\mathbf{x}) \ G(\mathbf{x}) \ B(\mathbf{x}) \ \alpha(\mathbf{x})]^{\top}. \quad (20)$$

After performing a J -level 3D discrete wavelet transform (DWT), we obtain a set of coefficients:

$$\{A_{j,\mathbf{o},\mathbf{k},c} \in \mathbb{R} \mid j, \mathbf{o}, \mathbf{k}, c\}, \quad c \in \{R, G, B, \alpha\}, \quad (21)$$

where j denotes the decomposition level, \mathbf{o} the subband orientation, and $\mathbf{k} = (k_x, k_y, k_z)$ the spatial index within the subband domain. Each coefficient $A_{j,\mathbf{o},\mathbf{k},c}$ thus encodes the contribution of channel c at spatial position \mathbf{k} in the subband oriented along \mathbf{o} at level j .

Gaussian Construction from a Single Coefficient. Following Section 4.2, each subband (j, \mathbf{o}) is associated with a canonical Gaussian $g(\mathbf{x}; \mathbf{u}_{j,\mathbf{o}}, \Sigma_{j,\mathbf{o}})$ (Eq. 15) and a 4D modulation vector $\mathbf{w}_{j,\mathbf{o}} \in \mathbb{R}^4$ (Eq. 17). For each coefficient at location \mathbf{k} , we compute an RGBA modulation vector:

$$\mathbf{p}_{j,\mathbf{o},\mathbf{k}} = \begin{bmatrix} |A_{j,\mathbf{o},\mathbf{k},R}| \\ |A_{j,\mathbf{o},\mathbf{k},G}| \\ |A_{j,\mathbf{o},\mathbf{k},B}| \\ |A_{j,\mathbf{o},\mathbf{k},\alpha}| \end{bmatrix} \odot \mathbf{w}_{j,\mathbf{o}}, \quad (22)$$

where \odot denotes element-wise multiplication. This vector encodes the local spectral energy of the RGBA channels, modulated by the channel weights. Multiplying the RGBA vector $\mathbf{p}_{j,\mathbf{o},\mathbf{k}}$ with the geometric Gaussian $g(\mathbf{x}; \mathbf{u}_{j,\mathbf{o}}, \Sigma_{j,\mathbf{o}})$ produces a 4D Gaussian primitive that represents the contribution of this wavelet coefficient:

$$s_{j,\mathbf{o}} \mathbf{p}_{j,\mathbf{o},\mathbf{k}} g(\mathbf{x}; \mathbf{u}_{j,\mathbf{o},\mathbf{k}}, \Sigma_{j,\mathbf{o}}). \quad (23)$$

Here, $s_{j,\mathbf{o}} = 2^{-3j/2}$ compensates for the intrinsic decay of the wavelet energy at coarser scales, while $\mathbf{u}_{j,\mathbf{o},\mathbf{k}}$ denotes the translated center of the canonical Gaussian, consistent with the canonical wavelet formulation in Eq. (12):

$$\mathbf{u}_{j,\mathbf{o},\mathbf{k}} = T_{2^j \mathbf{k} + \delta_{j,\mathbf{o}}}(\mathbf{u}_{j,\mathbf{o}}). \quad (24)$$

In summary, each wavelet coefficient gives rise to a Gaussian primitive parameterized as $(s_{j,\mathbf{o}} \mathbf{p}_{j,\mathbf{o},\mathbf{k}}, \mathbf{u}_{j,\mathbf{o},\mathbf{k}}, \Sigma_{j,\mathbf{o}})$, where the RGBA amplitude corresponds to $s_{j,\mathbf{o}} \mathbf{p}_{j,\mathbf{o},\mathbf{k}}$, the center to $\mathbf{u}_{j,\mathbf{o},\mathbf{k}}$, and the covariance to $\Sigma_{j,\mathbf{o}}$.

Gaussian Construction from a Subband. To construct the Gaussian representation of an entire subband (j, \mathbf{o}) , we first apply an adaptive filtering strategy (see supplementary material) to retain a sparse set of significant coefficients. Let $\Omega_{j,\mathbf{o}}$ denote the set of retained indices; each $\mathbf{k} \in \Omega_{j,\mathbf{o}}$ corresponds to a nonzero coefficient within the subband. The sparsified subband can be written as a linear combination of impulses (Eq. (9)): $\sum_{\mathbf{k} \in \Omega_{j,\mathbf{o}}} A_{j,\mathbf{o},\mathbf{k},c} e_{j,\mathbf{o},\mathbf{k}}(\boldsymbol{\kappa})$. Applying the IDWT to this expression yields the subband's spatial response:

$$\mathcal{W}^{-1} \left[\sum_{\mathbf{k} \in \Omega_{j,\mathbf{o}}} A_{j,\mathbf{o},\mathbf{k},c} e_{j,\mathbf{o},\mathbf{k}}(\boldsymbol{\kappa}) \right], \quad c \in \{r, g, b, \alpha\}. \quad (25)$$

By linearity of \mathcal{W}^{-1} , Eq. (25) can be rewritten as:

$$\sum_{\mathbf{k} \in \Omega_{j,\mathbf{o}}} A_{j,\mathbf{o},\mathbf{k},c} \mathcal{W}^{-1}[e_{j,\mathbf{o},\mathbf{k}}(\boldsymbol{\kappa})]. \quad (26)$$

Substituting the inverse kernel (Eq. 11) gives:

$$\sum_{\mathbf{k} \in \Omega_{j,\mathbf{o}}} A_{j,\mathbf{o},\mathbf{k},c} \hat{\psi}_{j,\mathbf{o},\mathbf{k}}(\mathbf{x}). \quad (27)$$

Approximating $\hat{\psi}_{j,\mathbf{o},\mathbf{k}}(\mathbf{x})$ by its optimal Gaussian form (Eq. 19) leads to:

$$\sum_{\mathbf{k} \in \Omega_{j,\mathbf{o}}} A_{j,\mathbf{o},\mathbf{k},c} w_{j,\mathbf{o}} g_{j,\mathbf{o},\mathbf{k}}(\mathbf{x}). \quad (28)$$

After applying attenuation compensation $s_{j,\mathbf{o}}$ and jointly arranging the four RGBA channels, we obtain a linear combination of Gaussian primitives (Eq. (23)):

$$\sum_{\mathbf{k} \in \Omega_{j,\mathbf{o}}} s_{j,\mathbf{o}} \mathbf{p}_{j,\mathbf{o},\mathbf{k}} g(\mathbf{x}; \mathbf{u}_{j,\mathbf{o},\mathbf{k}}, \Sigma_{j,\mathbf{o}}). \quad (29)$$

Hence, the spatial response of the sparsified subband can be represented by a set of Gaussian primitives:

$$\{s_{j,\mathbf{o}} \mathbf{p}_{j,\mathbf{o},\mathbf{k}}, \mathbf{u}_{j,\mathbf{o},\mathbf{k}}, \Sigma_{j,\mathbf{o}} \mid \mathbf{k} \in \Omega_{j,\mathbf{o}}\}. \quad (30)$$

Gaussian Construction from Subbands Aggregation.

By aggregating all subbands, we obtain a unified Gaussian-based volumetric representation that inherently preserves the coarse-to-fine information of the wavelet analysis:

$$RF(\mathbf{x}) \approx \sum_{j=1}^J \sum_{\mathbf{o}} \sum_{\mathbf{k} \in \Omega_{j,\mathbf{o}}} s_{j,\mathbf{o}} \mathbf{p}_{j,\mathbf{o},\mathbf{k}} g(\mathbf{x}; \mathbf{u}_{j,\mathbf{o},\mathbf{k}}, \Sigma_{j,\mathbf{o}}). \quad (31)$$

Each term in Eq. (31) serves a localized Gaussian primitive that contributes to the volumetric radiance field across scales and orientations. The resulting GS set is defined as:

$$\mathcal{G} = \{(s_{j,\mathbf{o}} \mathbf{p}_{j,\mathbf{o},\mathbf{k}}, \mathbf{u}_{j,\mathbf{o},\mathbf{k}}, \Sigma_{j,\mathbf{o}}) \mid \mathbf{k} \in \Omega_{j,\mathbf{o}}, j, \mathbf{o}\}, \quad (32)$$

where $\mathbf{u}_{j,\mathbf{o},\mathbf{k}}$, $\Sigma_{j,\mathbf{o}}$, $s_{j,\mathbf{o}} \mathbf{p}_{j,\mathbf{o},\mathbf{k}}$ provide the center, covariance matrix, color and opacity for initializing the 3DGs representation.

4.4. Image-space Gaussian Fine-tuning

To account for different visual modes in the volume, we generate multiple sets of radiance fields and their corresponding Gaussian representations using a series of transfer functions $\{TF_h\}$, where each TF_h is non-zero only within specific value intervals of the physical field F and zero elsewhere. This results in a set of radiance fields $RF_h = TF_h(F)$ for each mode h . For each radiance field RF_h , we render 64 images through volumetric integration, which provide supervision data for fine-tuning the initially constructed 3D Gaussian Set \mathcal{G}_h . The image-space loss is computed as in [26] and backpropagated to update \mathcal{G}_h . In practice, 5 transfer functions are selected for each volume. After fine-tuning, the Gaussians \mathcal{G}_h for each mode h can be either concatenated or separately rendered for global and local visibility, as described in [50].

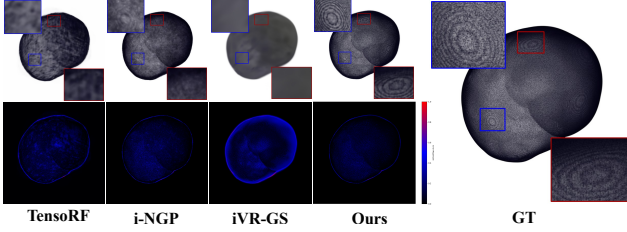


Figure 4. Qualitative comparison at an early training stage (0.5K). Our VBM-based Gaussians already captures fine structural details, demonstrating strong initialization and efficient convergence.

Table 1. Qualitative comparison on four datasets. PSNR/SSIM are reported at 4k and 15k iterations. Bold text indicates the best results, and underlined text represents the second-best.

Method	4k Iter		15k Iter		Time (min)
	PSNR	SSIM	PSNR	SSIM	
<i>Supernova</i>					
TensoRF	32.78	0.9022	34.01	0.9100	7.58
InstantNGP	33.43	0.9176	35.40	0.9207	<u>5.17</u>
3DGS	<u>38.20</u>	<u>0.9258</u>	39.11	0.9231	5.73
iVR-GS	38.02	0.9243	<u>39.23</u>	<u>0.9246</u>	6.18
Ours	39.09	0.9307	40.93	0.9273	5.06
<i>Colon Prone</i>					
TensoRF	26.40	0.8860	28.08	0.8859	12.65
InstantNGP	<u>27.81</u>	0.9109	29.75	0.9245	5.85
3DGS	26.65	<u>0.9123</u>	28.89	0.9192	7.93
iVR-GS	26.23	0.9105	28.91	0.9182	8.16
Ours	28.23	0.9208	<u>29.69</u>	<u>0.9198</u>	<u>7.86</u>
<i>Skull</i>					
TensoRF	25.97	0.925	28.00	0.9460	14.20
InstantNGP	<u>26.90</u>	0.9313	<u>27.90</u>	0.9488	4.70
3DGS	26.34	0.9372	27.50	0.9452	6.41
iVR-GS	26.35	<u>0.9376</u>	27.34	0.9446	7.45
Ours	27.18	0.9464	27.75	0.9454	<u>6.02</u>
<i>Foot</i>					
TensoRF	28.55	0.9219	30.75	0.9359	18.69
InstantNGP	27.26	<u>0.9294</u>	28.21	<u>0.9319</u>	<u>5.87</u>
3DGS	27.40	0.9328	28.01	0.9305	6.01
iVR-GS	27.38	0.9327	27.98	0.9292	7.92
Ours	<u>27.98</u>	0.9351	<u>28.23</u>	0.9313	5.85

5. Experiments

5.1. Datasets and Metrics

We evaluate our method on several representative volumetric datasets commonly used in scientific visualization. These include the *Supernova* volume (a 432^3 floating-point simulation from ECNR [49]), as well as three medical datasets from [28]: the *Colon Prone* CT scan ($512 \times 512 \times 463$, 16-bit intensity data), and two X-ray datasets, *Skull* and *Foot*, both of size 256^3 with 8-bit intensity values. These datasets span diverse modalities and resolutions, ranging from dense physical simulations to medical scans with varying dynamic ranges. For quantitative evaluation, we employ two standard image-quality metrics: PSNR and SSIM.

463, 16-bit intensity data), and two X-ray datasets, *Skull* and *Foot*, both of size 256^3 with 8-bit intensity values. These datasets span diverse modalities and resolutions, ranging from dense physical simulations to medical scans with varying dynamic ranges. For quantitative evaluation, we employ two standard image-quality metrics: PSNR and SSIM.

5.2. Implementation Details

Our framework is implemented in PyTorch with CUDA acceleration and uses PyWavelets for multi-scale decomposition. The Adam optimizer is adopted for all experiments. Reference volume renderings are generated in ParaView 5.12.1 with NVIDIA IndeX serving as the baseline renderer. All experiments are conducted on a workstation equipped with NVIDIA RTX 3090 GPUs.

5.3. Comparisons and Evaluations

We compare our method against state-of-the-art neural scene representation approaches, including TensoRF [7], Instant-NGP [38], 3DGS [26], and iVR-GS [50]. As summarized in Table 1, which presents the average metrics for each scene using 5 transfer functions TF_h , our framework consistently achieves higher PSNR and SSIM across all datasets while requiring significantly fewer training iterations. Notably, even at an early training stage (4k iterations), our model already produces comparable result to those of existing methods after full convergence. This demonstrates the fast convergence, representational efficiency, and stable optimization behavior of our formulation.

Qualitative comparisons are presented in Fig. 4 and Fig. 5, where our method yields sharper boundaries and more faithful volumetric structures than competing approaches, validating the effectiveness of the proposed wavelet-to-Gaussian mapping. For the *Supernova* dataset, our model utilizes approximately 1.8×10^5 Gaussian primitives and achieves real-time rendering performance of about 120 FPS on an RTX 3090 GPU.

5.4. Ablation Studies

We further analyze the contribution of each key component using the *Supernova* dataset under identical training conditions. Quantitative results are reported in Table 2, and qualitative comparisons are presented in Fig. 6.

(1) *w/o Transition Bank*. We disable the Wavelet-to-Gaussian Transition Bank by collapsing all covariances into a single shared isotropic matrix. Centers and opacity/appearance parameters remain unchanged, while each covariance is fixed as $\Sigma_{j,\mathbf{o}} = \sigma_{\text{iso}}^2 \mathbf{I}$ for all scales j and orientations \mathbf{o} , where σ_{iso} corresponds to the average spatial extent in the full model. Removing scale–orientation adaptivity produces smoother but noticeably blurrier results.

(2) *w/o Energy Projection*. Eliminating the energy conversion (by setting $\mathbf{w}_{j,\mathbf{o}} = 1$) causes global intensity imbal-

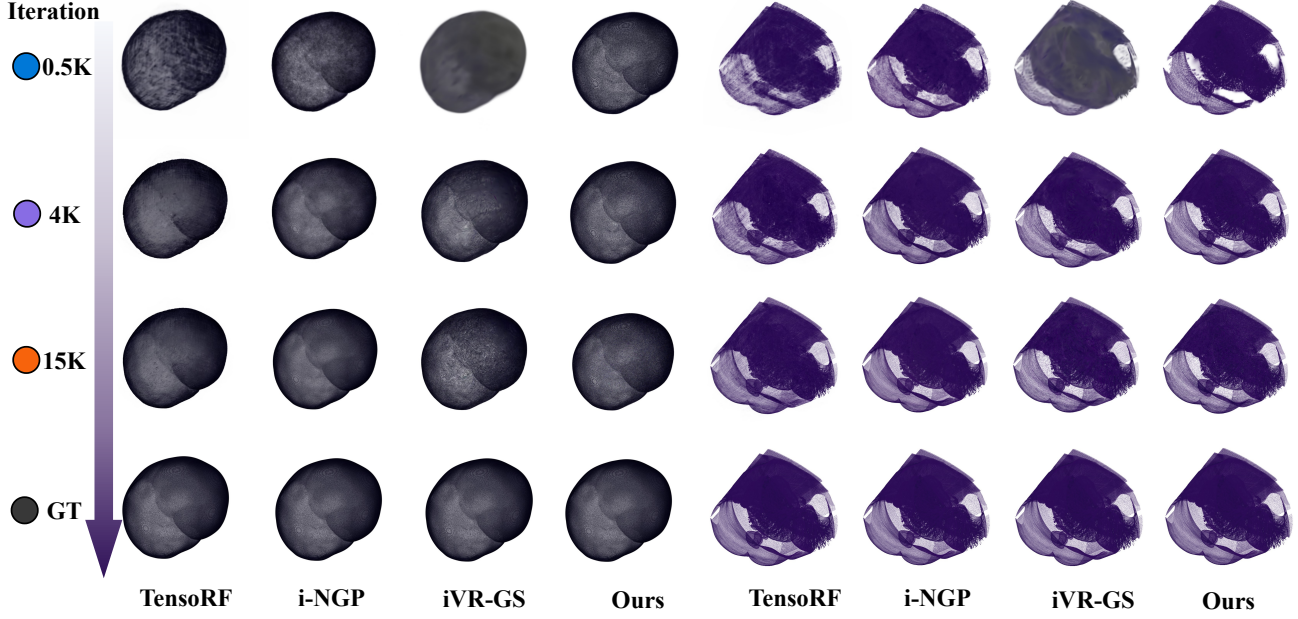


Figure 5. Qualitative comparison across training iterations. Our method rapidly refines structural details on both the Supernova simulation (left) and the Colon Prone CT volume (right), demonstrating consistent convergence across scientific and medical data.

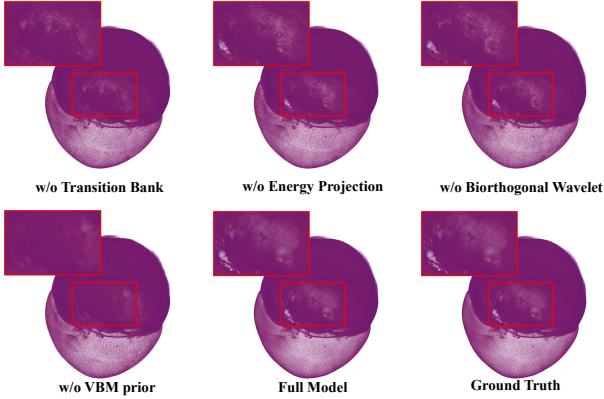


Figure 6. Qualitative ablation results of different variants on the *Supernova* dataset using a selected pink TF.

ance, highlighting the importance of proper energy scaling for stable photometric consistency.

(3) *w/o Biorthogonal Wavelet*. To evaluate sensitivity to the wavelet basis, we replace the default biorthogonal wavelet (`bior4.4`) with the Haar. Haar lacks the approximate translation consistency, leading to misaligned Gaussian centers and mild spatial fuzziness in the outputs.

(4) *w/o VBM Initialization*. We eliminate the VBM-based Gaussian initialization and randomly set all Gaussian parameters. This results in suboptimal optimization performance, highlighting the importance of the proposed

Table 2. Ablation results on the *Supernova* dataset, with PSNR (dB) and SSIM for quality evaluation.

Variant	PSNR	SSIM
w/o Transition Bank	30.88	0.9483
w/o Biorthogonal Wavelet	31.94	0.9505
w/o Energy Projection	32.18	0.9521
w/o VBM prior	30.84	0.9469
Full model	32.56	0.9543

framework in providing a crucial prior for efficient and stable training.

6. Conclusion

We introduced *VBM*, a unified framework that bridges volumetric wavelet analysis with 3D Gaussian Splatting for real-time volumetric visualization. Unlike heuristic or image-driven initialization strategies used in prior 3DGS-based methods, our approach establishes a principled analytical mapping from wavelet kernels to Gaussian primitives. By precomputing a compact Wavelet-to-Gaussian Transition Bank and formulating an analytical Gaussian construction strategy, VBM enables fast, accurate, and stable field-to-primitive conversion. A lightweight image-space fine-tuning further enhances visual fidelity without compromising efficiency. Extensive experiments demonstrate that VBM not only accelerates convergence and improves ren-

dering quality but also preserves volumetric semantics during conversion, achieving both analytical rigor and practical efficiency. Beyond these performance gains, our framework provides a new mathematical foundation that unifies multiresolution analysis with explicit scene representations. We believe this paradigm will inspire future research in structured neural representations, scientific visualization, and real-time rendering of complex volumetric phenomena.

References

- [1] Syed Twareque Ali, Jean-Pierre Antoine, and Jean-Pierre Gazeau. *Coherent States, Wavelets, and Their Generalizations*. Springer, 2nd edition, 2016. [2](#)
- [2] J-P Antoine and Pierre Vandergheynst. Wavelets on the 2-sphere: A group-theoretical approach. *Applied and Computational Harmonic Analysis*, 7(3):262–291, 1999. [2](#)
- [3] M. Antonini, M. Barlaud, P. Mathieu, and I. Daubechies. Image coding using wavelet transform. *IEEE Transactions on Image Processing*, 1(2):205–220, 1992. [2](#)
- [4] Tushar M Athawale, Zhe Wang, David Pugmire, Kenneth Moreland, Qian Gong, Scott Klasky, Chris R Johnson, and Paul Rosen. Uncertainty visualization of critical points of 2d scalar fields for parametric and nonparametric probabilistic models. *IEEE Transactions on Visualization and Computer Graphics*, 2024. [1](#)
- [5] David Bauer, Qi Wu, and Kwan-Liu Ma. Fovolnet: Fast volume rendering using foveated deep neural networks. *IEEE Transactions on Visualization and Computer Graphics*, 29(1):515–525, 2022. [2](#)
- [6] Tim Bruylants, Adrian Munteanu, and Peter Schelkens. Wavelet based volumetric medical image compression. *Signal processing: Image communication*, 31:112–133, 2015. [2](#)
- [7] Anpei Chen, Zexiang Xu, Andreas Geiger, Jingyi Yu, and Hao Su. Tensorf: Tensorial radiance fields. In *European conference on computer vision*, pages 333–350, 2022. [1, 2, 7](#)
- [8] Zikuan Chen and Ruola Ning. Breast volume denoising and noise characterization by 3d wavelet transform. *Computerized Medical Imaging and Graphics*, 28(5):235–246, 2004. [2](#)
- [9] Nikolay Chervyakov, Pavel Lyakhov, and Nikolay Nagornov. Analysis of the quantization noise in discrete wavelet transform filters for 3d medical imaging. *Applied Sciences*, 10(4):1223, 2020. [2](#)
- [10] Jaehoon Choi, Yonghan Lee, Hyungtae Lee, Heesung Kwon, and Dinesh Manocha. Meshgs: Adaptive mesh-aligned gaussian splatting for high-quality rendering. *arXiv preprint arXiv:2410.08941*, 2024. [2](#)
- [11] I. Daubechies. The wavelet transform, time-frequency localization and signal analysis. *IEEE Transactions on Information Theory*, 36(5):961–1005, 1990. [2](#)
- [12] Ingrid Daubechies. *Ten lectures on wavelets*. SIAM, 1992. [2, 5](#)
- [13] Landon Dyken, Andres Sewell, Will Usher, Steve Petruzza, and Sidharth Kumar. Volume encoding gaussians: Transfer function-agnostic 3d gaussians for volume rendering. *arXiv preprint arXiv:2504.13339*, 2025. [1, 2](#)
- [14] Thomas Fogal, Alexander Schiewe, and Jens Kruger. An analysis of scalable GPU-based ray-guided volume rendering. In *2013 IEEE Symposium on Large-Scale Data Analysis and Visualization*, pages 43–51, 2013. [2](#)
- [15] Sara Fridovich-Keil, Alex Yu, Matthew Tancik, Qinhong Chen, Benjamin Recht, and Angjoo Kanazawa. Plenoxels: Radiance fields without neural networks. In *Proceedings of the IEEE/CVF Conference on Computer Vision and Pattern Recognition (CVPR)*, pages 5501–5510, 2022. [1, 2](#)
- [16] Sara Fridovich-Keil, Giacomo Meanti, Frederik Rahbæk Warburg, Benjamin Recht, and Angjoo Kanazawa. K-planes: Explicit radiance fields in space, time, and appearance. In *Proceedings of the IEEE/CVF Conference on Computer Vision and Pattern Recognition (CVPR)*, pages 12479–12488, 2023. [1, 2](#)
- [17] Lin Gao, Jie Yang, Botao Zhang, Jiamu Sun, Yujie Yuan, Hongbo Fu, and Yu-Kun Lai. Real-time large-scale deformation of gaussian splatting. *ACM Transactions on Graphics*, 2024. [2](#)
- [18] Aman Ghasemzadeh and Hasan Demirel. 3d discrete wavelet transform-based feature extraction for hyperspectral face recognition. *Iet Biometrics*, 7(1):49–55, 2018. [2](#)
- [19] Enrico Gobbetti, Fabio Marton, and José Iglesias Gutián. A single-pass gpu ray casting framework for interactive out-of-core rendering of massive volumetric datasets. *The Visual Computer*, 24:797–806, 2008. [2](#)
- [20] Rafael C. Gonzalez and Richard E. Woods. *Digital Image Processing*. Prentice Hall, 3rd edition, 2008. [2](#)
- [21] Antoine Guédon and Vincent Lepetit. Sugar: Surface-aligned gaussian splatting for efficient 3d mesh reconstruction and high-quality mesh rendering. In *Proceedings of the IEEE/CVF Conference on Computer Vision and Pattern Recognition (CVPR)*, pages 5354–5363, 2024. [2](#)
- [22] Markus Hadwiger, Johanna Beyer, Won-Ki Jeong, and Hanspeter Pfister. Interactive volume exploration of petascale microscopy data streams using a visualization-driven virtual memory approach. *Visualization and Computer Graphics, IEEE Transactions on*, 18:2285–2294, 2012. [2](#)
- [23] Insung Ihm and Sanghun Park. Wavelet-based 3d compression scheme for interactive visualization of very large volume data. In *Computer Graphics Forum*, pages 3–15, 1999. [2](#)
- [24] Jakob Jakob, Markus Gross, and Tobias Günther. A fluid flow data set for machine learning and its application to neural flow map interpolation. *IEEE Transactions on Visualization and Computer Graphics*, 27(2):1279–1289, 2021. [1](#)
- [25] Eva Jerhotová, Jan Švihlík, and Aleš Procházka. Biomedical image volumes denoising via the wavelet transform. *Applied biomedical engineering*, pages 435–458, 2011. [2](#)
- [26] Bernhard Kerbl, Georgios Kopanas, Thomas Leimkühler, and George Drettakis. 3d gaussian splatting for real-time radiance field rendering. *ACM Transactions on Graphics*, 42(4), 2023. [1, 2, 3, 6, 7](#)
- [27] T Kim and Y Shin. An efficient wavelet-based compression method for volume rendering. In *Proceedings of the Seventh*

- Pacific Conference on Computer Graphics and Applications*, pages 147–156, 1999. 2
- [28] Pavol Klacansky. Open scivis datasets. <https://klacansky.com/open-scivis-datasets/>, 2017. 1, 7
- [29] Valentin Kraft, Florian Link, Andrea Schenk, and Christian Schumann. Adaptive illumination sampling for direct volume rendering. In *Computer Graphics International Conference*, pages 107–118, 2020. 2
- [30] Andreas Kurz, Thomas Neff, Zhaoyang Lv, Michael Zollhöfer, and Markus Steinberger. Adanerf: Adaptive sampling for real-time rendering of neural radiance fields. In *European Conference on Computer Vision*, pages 254–270, 2022. 2
- [31] Samuli Laine and Tero Karras. Efficient sparse voxel octrees. In *Proceedings of the 2010 ACM SIGGRAPH symposium on Interactive 3D Graphics and Games*, pages 55–63, 2010. 2
- [32] Guan Li, Yang Liu, Guihua Shan, Shiyu Cheng, Weiqun Cao, Junpeng Wang, and Ko-Chih Wang. Paramsdrag: Interactive parameter space exploration via image-space dragging. *IEEE Transactions on Visualization and Computer Graphics*, 2024. 1
- [33] Rui long Li, Hang Gao, Matthew Tancik, and Angjoo Kanazawa. Nerfacc: Efficient sampling accelerates nerfs. In *Proceedings of the IEEE/CVF International Conference on Computer Vision*, pages 18537–18546, 2023. 2
- [34] Yi Li, Eric Perlman, Minping Wan, Yunke Yang, Charles Meneveau, Randal Burns, Shiyi Chen, Alexander Szalay, and Gregory Eyink. A public turbulence database cluster and applications to study lagrangian evolution of velocity increments in turbulence. *Journal of Turbulence*, 9:N31, 2008. 1
- [35] Stéphane Mallat. *A wavelet tour of signal processing*. Elsevier, 1999. 2
- [36] N. Max. Optical models for direct volume rendering. *IEEE Transactions on Visualization and Computer Graphics*, 1(2): 99–108, 1995. 1, 2
- [37] Ben Mildenhall, Pratul P Srinivasan, Matthew Tancik, Jonathan T Barron, Ravi Ramamoorthi, and Ren Ng. Nerf: Representing scenes as neural radiance fields for view synthesis. *Communications of the ACM*, 65(1):99–106, 2021. 1, 2
- [38] Thomas Müller, Alex Evans, Christoph Schied, and Alexander Keller. Instant neural graphics primitives with a multiresolution hash encoding. *ACM Transactions on Graphics*, 41(4):1–15, 2022. 1, 2, 7
- [39] Simon Niedermayr, Christoph Neuhauser, Kaloian Petkov, Klaus Engel, and Rüdiger Westermann. Application of 3D Gaussian Splatting for Cinematic Anatomy on Consumer Class Devices. In *Vision, Modeling, and Visualization*, 2024. 1
- [40] Martin Pätzold and Andreas Kolb. Grid-free out-of-core voxelization to sparse voxel octrees on gpu. In *Proceedings of the 7th conference on high-performance graphics*, pages 95–103, 2015. 2
- [41] Aleš Procházka, Lucie Gráfová, Oldrich Vyšata, and Neurocenter Caregroup. Three-dimensional wavelet transform in multi-dimensional biomedical volume processing. In *Proc. of the IASTED International Conference on Graphics and Virtual Reality*, page 268, 2011. 2
- [42] Manel Rhif, Ali Ben Abbes, Imed Riadh Farah, Beatriz Martínez, and Yanfang Sang. Wavelet transform application for/in non-stationary time-series analysis: A review. *Applied sciences*, 9(7):1345, 2019. 2
- [43] Johannes L. Schönberger and Jan-Michael Frahm. Structure-from-motion revisited. In *Proceedings of the IEEE/CVF Conference on Computer Vision and Pattern Recognition (CVPR)*, pages 4104–4113, 2016. 1
- [44] Andres Sewell, Landon Dyken, et al. High-quality approximation of scientific data using 3d gaussian splatting. *Proceedings of the IEEE Symposium on Large Data Analysis and Visualization (LDAV)*, pages 73–74, 2024. 1, 2
- [45] Elias M. Stein and Rami Shakarchi. *Real Analysis: Measure Theory, Integration, and Hilbert Spaces*. Princeton University Press, 2009. 5
- [46] Elias M Stein and Rami Shakarchi. *Fourier analysis: an introduction*. Princeton University Press, 2011. 2
- [47] Cheng Sun, Min Sun, and Hwann-Tzong Chen. Direct voxel grid optimization: Super-fast convergence for radiance fields reconstruction. In *2022 IEEE/CVF Conference on Computer Vision and Pattern Recognition*, pages 5449–5459, 2022. 1
- [48] Jianxin Sun, David Lenz, Hongfeng Yu, and Tom Peterka. Make the fastest faster: Importance mask for interactive volume visualization using reconstruction neural networks. *arXiv preprint arXiv:2502.06053*, 2025. 2
- [49] Kaiyuan Tang and Chaoli Wang. ECNR: Efficient compressive neural representation of time-varying volumetric datasets. In *Proceedings of IEEE Pacific Visualization Conference*, pages 72–81, 2024. 2, 7
- [50] Kaiyuan Tang, Siyuan Yao, and Chaoli Wang. ivr-gs: Inverse volume rendering for explorable visualization via editable 3d gaussian splatting. *arXiv preprint arXiv:2504.17954*, 2025. 1, 2, 6, 7
- [51] Christopher C. Tanner, Christopher J. Migdal, and Michael T. Jones. The clipmap: a virtual mipmap. In *Proceedings of the 25th Annual Conference on Computer Graphics and Interactive Techniques*, page 151–158, 1998. 2
- [52] Ivan Viola, Armin Kanitsar, and Meister Eduard Gröller. Importance-driven volume rendering. In *IEEE visualization 2004*, pages 139–145, 2004. 2
- [53] Joanna Waczyńska, Piotr Borycki, Sławomir Tadeja, Jacek Tabor, and Przemysław Spurek. Games: Mesh-based adapting and modification of gaussian splatting. *arXiv preprint arXiv:2402.01459*, 2024. 2
- [54] Sebastian Weiss and Rüdiger Westermann. Differentiable direct volume rendering. *IEEE Transactions on Visualization and Computer Graphics*, 28(1):562–572, 2021. 1
- [55] Alex Yu, Rui long Li, Matthew Tancik, Hao Li, Ren Ng, and Angjoo Kanazawa. Plenoctrees for real-time rendering of neural radiance fields. In *Proceedings of the IEEE/CVF International Conference on Computer Vision*, pages 5752–5761, 2021. 1

- [56] Zheng Zhang, Dongyue Guo, Shizhong Zhou, Jianwei Zhang, and Yi Lin. Flight trajectory prediction enabled by time-frequency wavelet transform. *Nature Communications*, 14(1):5258, 2023. [2](#)
- [57] Junsheng Zhou, Weiqi Zhang, Baorui Ma, Kanle Shi, Yu-Shen Liu, and Zhizhong Han. Udiff: Generating conditional unsigned distance fields with optimal wavelet diffusion. In *Proceedings of the IEEE/CVF Conference on Computer Vision and Pattern Recognition (CVPR)*, pages 21496–21506, 2024. [2](#)